Applied Surface Science 423 (2017) 743–751

Contents lists available at ScienceDirect

Applied Surface Science

journal homepage: www.elsevier.com/locate/apsusc

Full Length Article

rGO-ZnO nanocomposites for high electrocatalytic effect on water oxidation obtained by microwave-hydrothermal method

Fernanda C. Romeiro[a], Mônica A. Rodrigues[a], Luiz A.J. Silva[a], Ariadne C. Catto[b], Luis F. da Silva[c], Elson Longo[d], Edson Nossol[a], Renata C. Lima[a,*]

[a] Instituto de Química, Universidade Federal de Uberlândia, 38400-902, Uberlândia, MG, Brazil
[b] LIEC, Instituto de Química, Universidade Estadual Paulista, 14800-900, Araraquara-SP, Brazil
[c] Departamento de Física, Universidade Federal de São Carlos, 13565-905, São Carlos, SP, Brazil
[d] LIEC, Departamento de Química, Universidade Federal de São Carlos, 13565-905, São Carlos, SP, Brazil

ARTICLE INFO

Article history:
Received 31 March 2017
Received in revised form 14 June 2017
Accepted 21 June 2017
Available online 27 June 2017

Keywords:
Zinc oxide
Graphene
Nanoparticles
Microwave
Electrocatalysis
O_2 evolution

ABSTRACT

Reduced graphene oxide-zinc oxide (rGO-ZnO) nanocomposites were successfully synthesized using a facile microwave-hydrothermal method under mild conditions, and their electrocatalytic properties towards O_2 evolution were investigated. The microwave radiation played an important role in obtainment of well dispersed ZnO nanoparticles directly on reduced graphene oxide sheets without any additional reducing reagents or passivation agent. X-ray diffraction (XRD), Raman and infrared spectroscopies indicated the reduction of GO as well as the successful synthesis of rGO-ZnO nanocomposites. The chemical states of the samples were shown by XPS analyses. Due to the synergic effect, the resulting nanocomposites exhibited high electronic interaction between ZnO and rGO sheets, which improved the electrocatalytic oxidation of water with low onset potential of 0.48 V (vs. Ag/AgCl) in neutral pH and long-term stability, with high current density during electrolysis. The overpotential for water oxidation decreased in alkaline pH, suggesting useful insight on the catalytic mechanism for O_2 evolution.

1. Introduction

Development of efficient catalysts for the splitting of water to produce hydrogen (H_2) and oxygen (O_2) is one of the most promising challenges for producing sustainable energy with minimal environmental impacts [1,2]. However, the water splitting – *chemical processes that involves proton reduction and water oxidation* – is mainly hindered by dioxygen O_2 evolution, which involves significant molecular rearrangements and requires large overpotential [3,4]. In this process, H_2O is the renewable multi-electron source, providing a total of four electrons and four protons to form oxygen–oxygen bonds [5]. Energy demands motivated the development of promising energy conversion devices with low-cost, that operate at lower overpotential and present selectivity, high speed and stability [6–8]. Metallic oxides, such as Ir_2O and Ru_2O have been employed to enhance the catalytic performance for oxygen evaluation catalysts with low overpotential, especially in acidic conditions [9]. However, these catalysts suffer from their high cost and low elemental abundance as well as poor long-term stability in alkaline media [4]. Suntivich *et al.* [10] showed that perovskite oxide catalysts can enhance the intrinsic activity for the oxygen evaluation in alkaline solution due to a near-unity occupancy of the e_g orbital of surface transition-metal ions. Given the diversity of materials studied for energy conversion and storage applications, the graphene structure has attracted attention due to large specific surface area, high intrinsic mobility, excellent mechanical strength and thermal conductivity [11–14]. One possible route to harnessing these properties for catalyst applications would be to use the graphene as the support material due to excellent electronic communication achieved between the catalyst and the graphene in addition to other synergistic effects [15–19]. Among oxides, the well-recognized semiconducting ZnO presents high exciton binding energy (60 meV) and wide band-gap (3.37 eV), which allow a variety of uses in electrochemical properties [20,21], magnetic compounds [22], solar cells [23], photocatalysts [24–26] and gas sensing devices [27]. According to Osterloh [28], to facilitate water oxidation, the semiconductor band-gap energy must exceed the oxidation potential of water (~1.23 eV), what enables ZnO for such application. In view of the notable individual properties of graphene and ZnO, attempts to combine these compounds to obtain hybrid materials with superior electrochemical properties have been reported [29–31]. The microwave-assisted hydrothermal (MAH) method has been

* Corresponding author.
E-mail address: rclima@ufu.br (R.C. Lima).

http://dx.doi.org/10.1016/j.apsusc.2017.06.221
0169-4332/

demonstrated efficiency in the preparation of organic and inorganic compounds. The use of MAH route provides uniform heating, high reaction rate, rapid nucleation and growth of particles, which can reduce the reaction time [20,32]. Besides allowing the formation of ZnO particles [33], the microwaves can be absorbed by graphene oxide (GO), which results in a local heating effect on GO nanosheets which facilitates their reduction [34].

In this work we report a simple one-step synthesis of pure ZnO and rGO-ZnO nanocomposites for electrochemical water oxidation using facile MAH method without reducing agents. The MAH method promoted the formation of ZnO nanoparticles dispersed on rGO sheets by the strong local heating, leading to graphene oxide reduction. The rGO-ZnO nanocomposites showed enhanced H_2O oxidizing power at lower potential for the nanocomposite with higher quantity of rGO. This fact was attributed to excellent electron transport and the reduction of charge carrier recombination resulting from the use of the carbonaceous material. The structural properties of samples were investigated using powder X-ray diffraction (XRD), Raman and infrared spectroscopies, X-ray photoelectron spectroscopy (XPS), field emission scanning electron microscope (FE-SEM) and transmission electron microscope (TEM). Electrochemical characterization was performed using cyclic voltammetry, chronoamperometry and electrochemical impedance spectroscopy.

2. Experimental

2.1. Synthesis of rGO-ZnO nanocomposites

The ZnO was obtained from the addition of 5.0×10^{-3} mol of $Zn(CH_3COO)_2$ in 40 mL of distilled water under constant stirring. KOH solution (3.0 mol L^{-1}) was added until a pH = 10.5 was attained. Graphite oxide was obtained from natural graphite by the Hummers method [35]. Graphene oxide was prepared using dispersions containing 8.0 and 16 mg of graphite oxide in 20 mL of distilled water with posterior overnight stirring. Subsequently, ultrasonic treatment for 30 min to form a light brown suspension. After, a suspension of $Zn(CH_3COO)_2$ in 20 mL of distilled water, obtained from ultrasonic treatment for 30 min, was added into the GO dispersion under magnetic stirring. The final solutions were transferred into a Teflon autoclave, and then sealed and placed in the microwave-assisted equipment. All solutions were annealed for 8 min at 100 °C. The precipitate powder was washed several times with deionized water and ethanol. Finally, the powder samples were dried at 60 °C for 2 h in air atmosphere. For simplicity, the nanocomposites prepared from addition of 8.0 and 16 mg of GO were referred as 8rGO-ZnO and 16rGO-ZnO, respectively.

2.2. rGO-ZnO nanocomposite film preparation

The nanocomposite films were prepared based on interfacial method [36–38]. Briefly, 3.0 mg of rGO-ZnO nanocomposite was added in 20 mL of water under strong magnetic stirring for 30 min. The solution was maintained under ultrasound bath for 30 min. Then, the resulting mixture was transferred to a 50-mL round-flask containing 20 mL of toluene. The two-phase system was maintained under strong magnetic stirring for 24 h. After 24 h, the magnetic stirring stopped, and the transparent film obtained in interface was deposited onto the FTO surface and dried at 70 °C for 2 h in air atmosphere.

2.3. Electrochemical studies

Cyclic voltammetry (CV) and chronoamperometry analyses were carried out using a PGSTAT12 Autolab potentiostat equipped with a conventional one-compartment three-electrode cell containing the working nanocomposite film electrode, a platinum wire as a counter electrode and an Ag/AgCl (3.0 mol L^{-1} KCl) as reference electrode. Electrocatalytic activity for water oxidation was measured in 0.1 mol L^{-1} phosphate buffer (pH 7.0), and either 3 mol L^{-1} KOH was used for pH adjustment in pH dependent measurements. Cyclic voltammetry (CV) of the electrode was obtained at a scan rate of 50 mV s^{-1} in the potential range of 0.4 to 1.4 V. Chronoamperometry measurements were conducted using 0.1 mol L^{-1} phosphate buffer (pH 7.0) as the electrolyte. Electrochemical impedance spectroscopy experiments were carried out using an Autolab PGSTAT 128N potenciostat with FRA2 module. The AC signal was collected using an amplitude of 10 mV (rms), and varying the frequency in the 0.01–30 kHz range. All the experiments were performed at ambient temperature. 2.4. Physical characterization rGO-ZnO nanocomposites powders were characterized by X-ray diffraction (Shimadzu XRD 6000) with a Cu Kα radiation source (λ = 1.5406 Å). Scanning electron microscopy (SEM) analysis were performed using a Mira field emission gun FEG-SEM (TESCAN, BrnoKohoutovice, Czech Republic) operated at 10 kV. The samples were dispersed in ethanol and drop-casted on silicon substrates. Transmission electron microscopy (TEM) analyses of the nanocomposites were performed using a FEI microscope Tecnai G2TF20 operating at 25 kV in different magnifications. Raman spectra at room temperature were recorded using a Renishaw Raman spectroscopy microscope (Gloucestershire, United Kingdom) with 1 mm spot and using a 514.5 nm He-Ne laser with an incidence power of 2 mW. The infrared spectra were measured from powder samples diluted in KBr on an FTIR Bomem-Michelson 102 spectrometer in the 4000–400 cm^{-1} region. X-ray photoelectron spectroscopy (XPS) analyses were performed on a Scienta Omicron, model ESCA± spectrometer using monochromatic AlKα (1486.6 eV) radiation. Peak decomposition was performed using a Gaussian-Lorentzian line shape with a Shirley nonlinear sigmoid-type baseline. The binding energies were corrected for charging effects by assigning a value of 284.8 eV to the adventitious C 1 s line. The data were analyzed using CasaXPS software (Casa Software Ltd., U.K.).

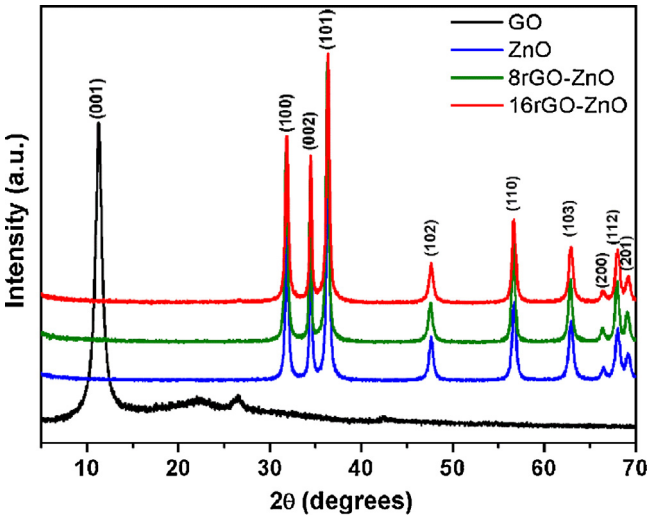

Fig. 1. XRD patterns of the GO, ZnO and rGO-ZnO samples.

3. Results and discussion

The XRD patterns of the GO, ZnO and rGO-ZnO samples are shown in Fig. 1. The XRD pattern of GO shows a typical diffraction peak at 2Θ = 11.28° attributed to the (001) lattice plane and narrow peaks at 26.46° and 42.47° attributed to (002) and (101) planes,

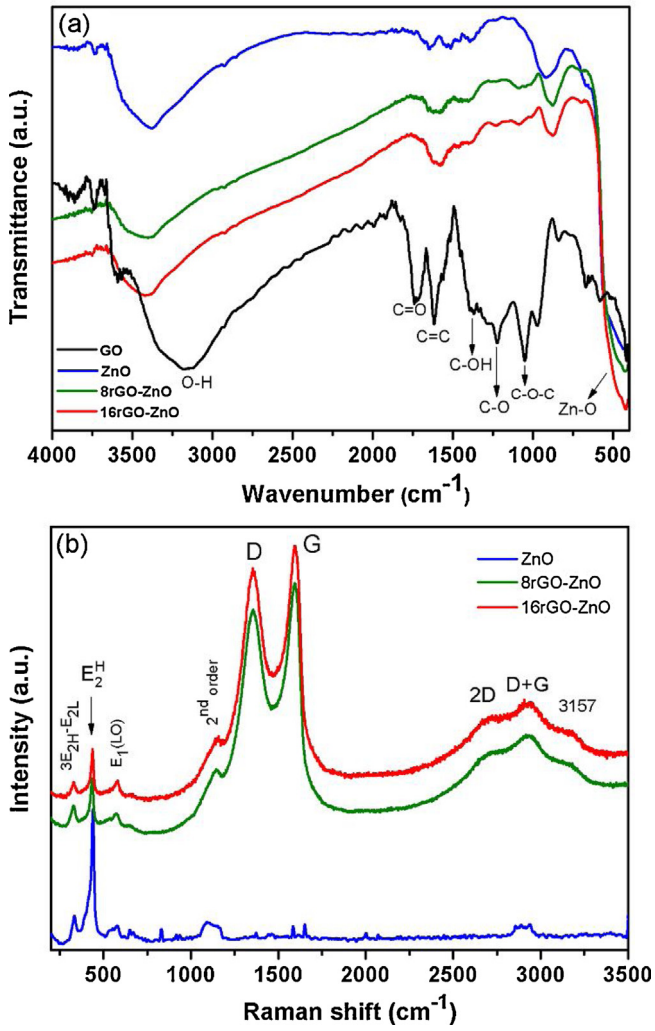

Fig. 2. (a) FTIR spectra and (b) Raman spectra of the ZnO and rGO-ZnO samples.

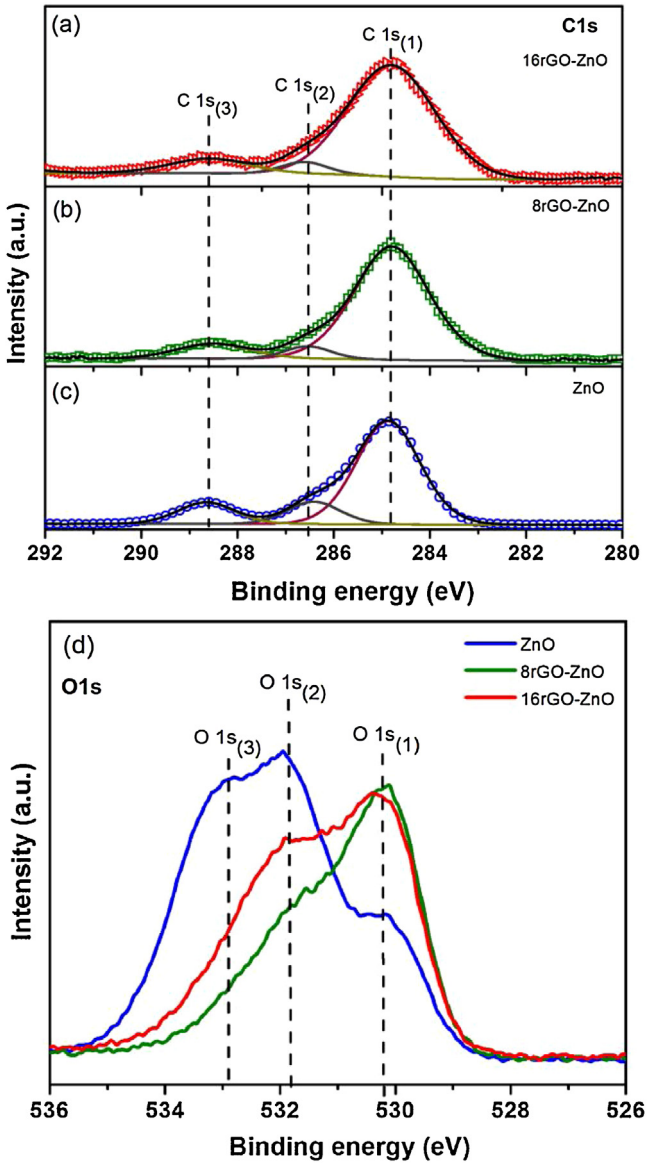

Fig. 3. XPS spectra of (a) 16rGO-ZnO, (b) 8rGO-ZnO, (c) pure ZnO samples in the C 1 s region and (d) high-resolution O 1 s spectrum for rGO-ZnO samples.

respectively. ZnO and rGO-ZnO samples show the single pure phase of wurtzite structure – hexagonal symmetry and P63mc space group. The absence of peaks from GO in the rGO-ZnO nanocomposites in the XRD patterns is an indicative that the reduction of GO to rGO under microwave hydrothermal conditions has been occurred.

FTIR spectra of GO, ZnO and rGO-ZnO samples are shown in Fig. 2(a). For GO sample is observed a broad band centered at 3172 cm^{-1} attributed to the O—H stretching. The bands at 1723, 1620, 1368 cm^{-1} were assigned to the C=O stretching, sp^2 hybridized C=C group and C—OH deformation, respectively [39]. The absorption bands at 1056 and 1225 cm^{-1} are attributed to the stretching of C—O—C and C=O of COOH groups situated on GO sheets, respectively [40,41]. The bands of GO disappear in the FTIR spectra of the rGO-ZnO nanocomposites, confirming the reduction of GO in agreement with the XRD results [41]. In addition, the FTIR spectra of the pure ZnO and rGO-ZnO showed a band around 437 cm^{-1}, corresponding to the E_{2H} mode of hexagonal ZnO [42].

In Fig. 2(b) is displayed the Raman spectra of ZnO and rGO-ZnO samples. The ZnO and rGO-ZnO samples presented a band at around 438 cm^{-1} corresponding to E_2(high) mode, which is characteristic of the ZnO wurtzite structure [43]. The Raman modes at 330 and 578 cm^{-1} are ascribed to $3E_{2H}$-E_{2L} and E_1(LO) phonon modes, also belonging to ZnO [44]. The broad band located at around 1147 cm^{-1} is related to $2A_1$(LO) and $2E_1$(LO) modes at the point of the Brillouin zone of ZnO [44]. The spectrum of rGO-ZnO nanocomposites are consisted of additional bands related to reduced graphene structure. The two prominent bands for rGO-ZnO nanocomposites at 1355 cm^{-1} (D band) and 1592 cm^{-1} (G band) correspond to the carbon–carbon vibrations that become actives due to defect states in graphene sheets and the E_{2g} phonon of sp^2 bonds of carbon atoms, respectively [45]. So, the intensity ratio I_D/I_G can be used as an analysis factor for disorder evaluation in carbonaceous materials. It is noted for 8rGO-ZnO composite that this value (3.17) is higher than that of the 16rGO-ZnO composite (3.09), which suggest the presence of more structural defects in the rGO lattice due to reduction of GO in presence of a major ratio of ZnO nanoparticles [46]. The band around 2706 cm^{-1} (2D) can be related to second order of zone boundary phonons [47], and the band at 2926 cm^{-1} associates with the D + G band vibration [41]. Ghosh, *et al.* [45] attributed the appearance of the bands at ~3157 cm^{-1} to the overtone of intra-valley double resonance effect. The nanocomposites presented vibrations modes related to ZnO and rGO, indicating the successful synthesis of the materials, in good accordance with XRD and infrared results.

The XPS survey spectra of pure ZnO, 8rGO-ZnO and 16 rGO-ZnO samples revealed only the presence of Zn, O and C elements, as seen

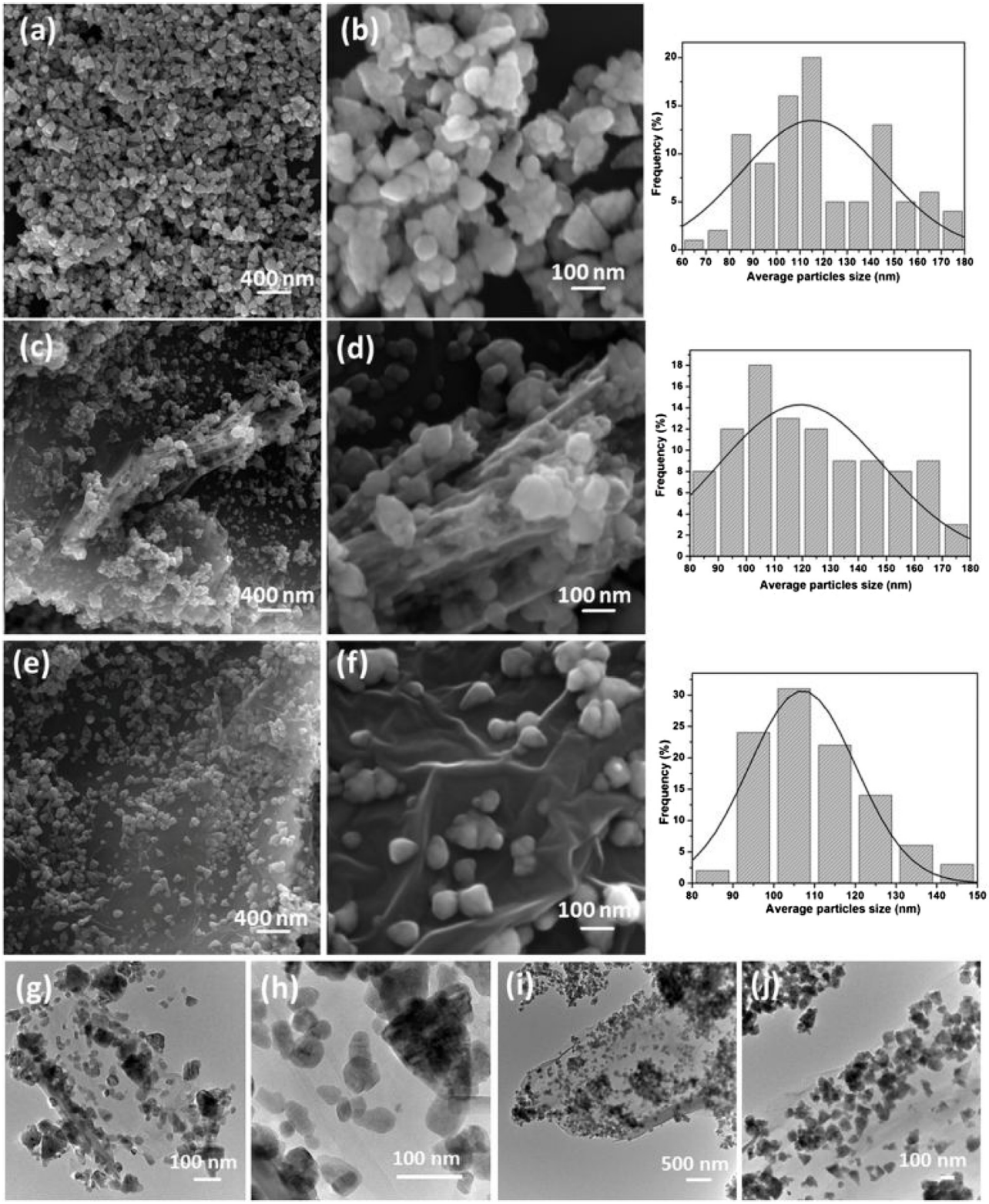

Fig. 4. FE-SEM images of nanocomposites obtained by the MAH method (a–b) pure ZnO (c–d) 8rGO-ZnO and (e–f) 16rGO-ZnO (the histograms are on the right side of the corresponding FE-SEM images). TEM images of nanocomposites (g–h) 8rGO-ZnO and (i–j) 16rGO-ZnO.

in Fig. S1(a) (Supplementary Material). The high-resolution Zn 2p spectra were measured for all samples, and the comparison of the high resolution Zn 2p 3/2 XPS spectra revealed similar results for pure ZnO and rGO-ZnO samples, i.e., the predominance of $Zn^{2\pm}$ (Fig. S1(b); Supplementary Material).

Fig. 3 presents the high-resolution XPS spectra of C 1s, and O 1s. First, the high-resolution carbon region was deconvoluted into three types of components, labeled as $C1s_{(1)}$, $C1s_{(2)}$ and $C1s_{(3)}$. The main peak at around 284.8 eV ($C1s_{(1)}$), correspond to the C—C bonds, while the other two peaks with a binding energy of approximately 286.1 eV and 288.7 eV are ascribed to oxygen-containing functional

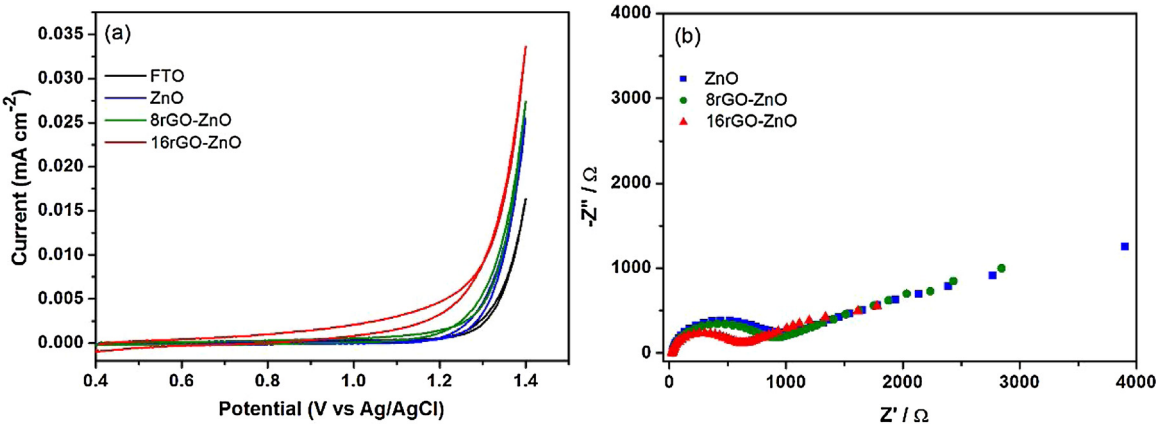

Fig. 5. (a) CVs of the FTO background (black), ZnO and rGO-ZnO nanocomposites in phosphate buffer, pH = 7 and (b) Nyquist plots obtained for the prepared films. Electrolyte: 1.0 mmol L^{-1} ferro/ferricyanide in 0.1 mol L^{-1} KCl.gr5gr5

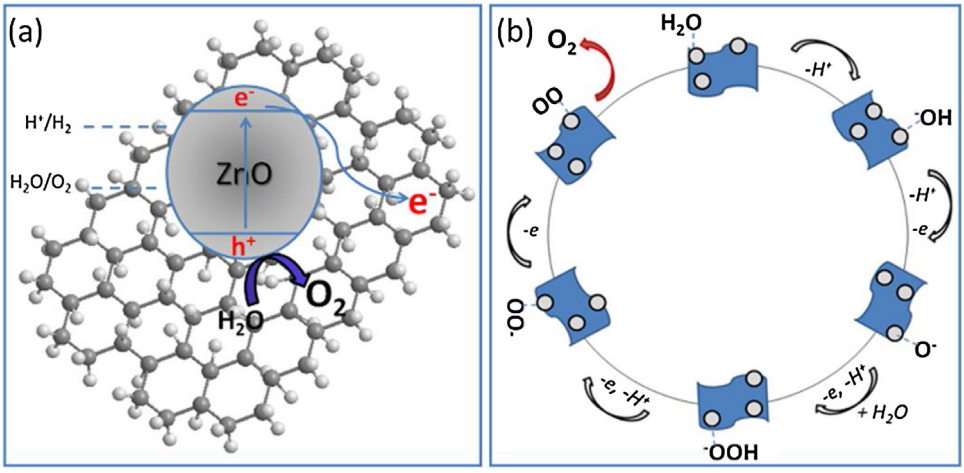

Fig. 6. Schematic representation of (a) electron transfer process (b) mechanism for water oxidation on rGO-ZnO electrocatalyst film.

groups, as C—O—C and O—C=O, respectively[48–50]. Furthermore, considering the XPS peak areas ratio (Table S1; Supplementary Material), the results showed that rGO-ZnO samples presented a lower contribution of oxygen containing bond due the high reduction degree of the GO in rGO-ZnO nanocomposites [48,49,51]. The XPS high-resolution O 1 s spectra are displayed in Fig. 3(d). The analysis of these spectra revealed the presence of three oxygen species, labeled as $O1s_{(1)}$, $O1s_{(2)}$ and $O1s_{(3)}$. The lower energy peak at around 530.0 eV ($O1s_{(1)}$), correspond to O^{2-} ions in lattice connected with Zn ions, while the second peak at around 531.7 eV ($O1s_{(2)}$) was attributed to oxygen species weakly adsorbed on surface in forms of —OH and carbonate. The third peak located at approximately 533.0 eV was assigned to water molecules, C—OH and/or C—O—C groups [50,52,53]. In addition, the XPS peak areas ratio evidenced a significant decrease of $O1s_{(3)}$ component for 8rGO-ZnO and 16rGO-ZnO samples, which is in accordance with XPS high-resolution C 1 s spectra. The deconvoluted O 1 s XPS spectra of all samples are displayed in Fig. S1(c–e) (Supplementary Material).

Fig. 4 shows the FE-SEM and TEM images and the respective histograms related with the average particle size distributions of the pure ZnO and rGO-ZnO nanocomposites. The FE-SEM images show that the pure ZnO presented irregular elongated shapes and agglomerates with particle size of 122 nm (Fig. 4(a–b)). The size of ZnO particles decreased with the increase of rGO content in 16rGO-ZnO (110 nm) nanocomposites. Besides, the ZnO particles become well dispersed on the rGO and present particles with regular shape decorating rGO sheets (Fig. 4(c-f)). The FE-SEM images show an effective contact between ZnO nanoparticles and rGO, which can improve electronic interaction between the components [54]. TEM micrographs of 8rGO-ZnO and 16rGO-ZnO samples are displayed in Fig. 4(g–j). The ZnO nanoparticles exhibited an irregular shape with a large size distribution, in accordance with FE-SEM analyses. Furthermore, it was also observed that the transparent rGO sheets were successful decorated by the ZnO nanostructures in both samples, suggesting the formation of rGO-ZnO nanocomposites.

The synthesis process used in this work represents an attractive route for controlling the nanoparticles morphology and size, with efficient nucleation. Moreover, the homogeneous particles growing at low temperatures and in short reaction times offers high mobility of dissolved ions and molecules [55], with simultaneous reducing of graphene oxide to rGO by MAH treatment. In a polar solvent and under thermal treatment, the reduction of graphene oxide can be facilitated with water acting as a reducing agent, which was observed by Van Hoa, *et al.* [56]. In the synthesis process, Zn^{2+} ions react with the OH^- groups forming the precipitates of $Zn(OH)_2$, which in excess of OH^-, dissolve and react with these ions forming $[Zn(OH)_4]^{2-}$, which is stable at high pH. When the concentration of Zn^{2+} and OH^- reaches the saturation degree of zinc oxide, the formation of the first ZnO nuclei initiates, which leads to the crystal growth [57]. In presence of GO precursor, the large number of polar groups in the carbon material act as anchors to enable the formation of ZnO nanoparticles, promoting the formation of homogeneous in

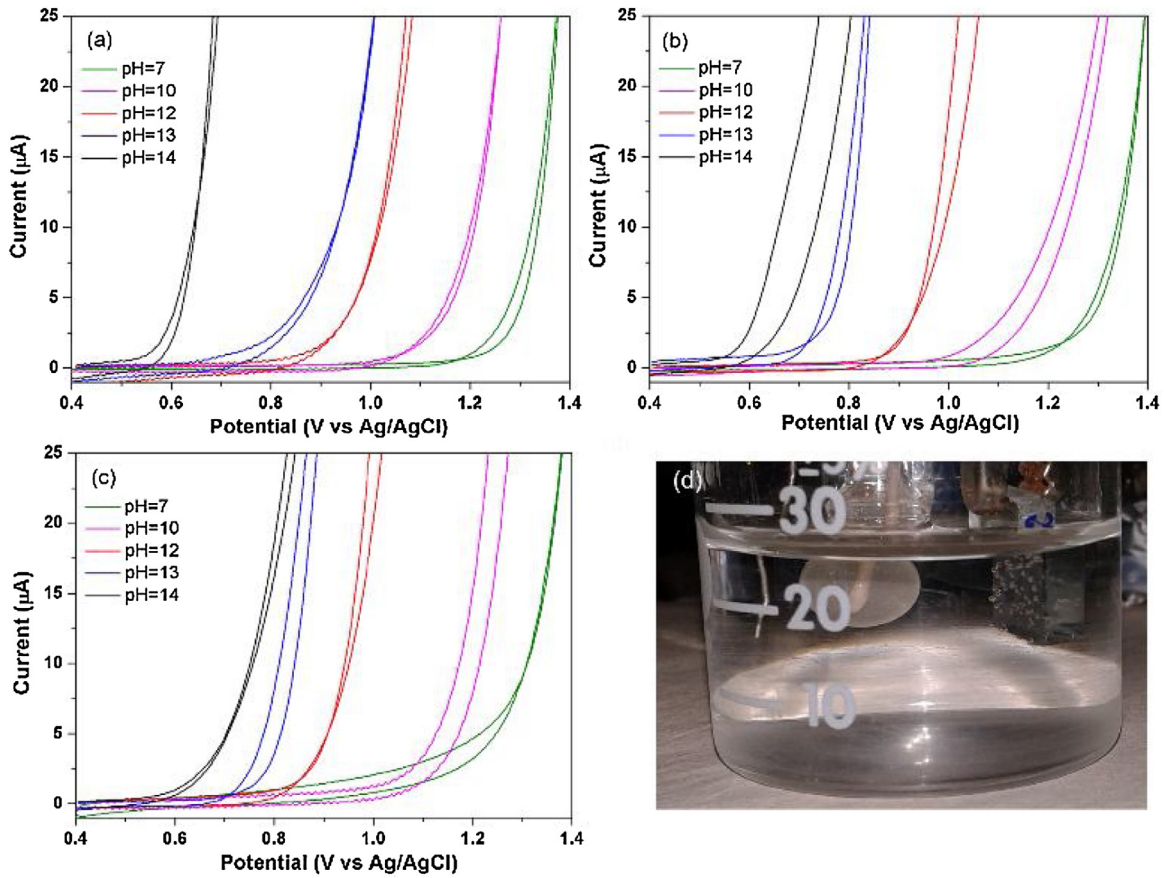

Fig. 7. CVs of 1 in aqueous solutions at different pH values (7, 10, 12, 13 and 14) (measured at i = 25 μA) (a) ZnO pure (b) 8rGO-ZnO and (c) 16rGO-ZnO nanocomposites films (d) O_2 gas bubbles formed on the 16rGO-ZnO film during application of 1.40 V.

size and well dispersed ZnO nanoparticles decorating the surface of GO sheets [58].

The electrochemical activity of pure ZnO and rGO-ZnO nanocomposite films for water oxidation was investigated by cyclic voltammetry in a 0.1 mol L^{-1} phosphate buffer (pH = 7.0). Cyclic voltammetric studies obtained for FTO background are also included for comparison. Fig. 5(a) reveals that 16rGO-ZnO nanocomposite film exhibits a significant electrocatalytic effect for oxygen evolution reaction, with an onset potential at 0.48 V (vs. Ag/AgCl), lower than thermodynamic requirement for water oxidation (0.62 V vs. Ag/AgCl at pH = 7) [59], while this process for the ZnO film occurs at around 1.19 V. In addition, the 16rGO-ZnO nanocomposite films exhibited higher current when compared to pure ZnO film (Fig. 5(a)). In order to verify the influence of rGO on the electrical properties of ZnO films, EIS experiments were performed. The Nyquist spectra, Fig. 5(b) obtained for both electrodes (pure ZnO, 8rGO-ZnO and 16rGO-ZnO) showed well-defined semicircles from which the values of the ohmic (R_Ω) and the charge transfer (R_{ct}) resistances were calculated. By comparing the profile of these semicircles, it is observed that the presence of carbonaceous material provides a decrease in impedance charge transfer resistances for 8rGO-ZnO (R_Ω = 25.6 Ω, R_{ct} = 839.8 Ω) and 16rGO-ZnO (R_Ω = 19.8 Ω, R_{ct} = 570.8 Ω) films compared with pure ZnO (R_Ω = 26.8 Ω, R_{ct} = 914.1 Ω). These results are in agreement with superior electrical contact induced by synergistic interaction of ZnO nanoparticles with the rGO sheets.

These results are more impressive when confronted with other electroactive materials and its respectively water oxidation potentials in neutral conditions: Zhao et al., 0.858 V [60]; Han, et al., ~1.00 V [61]; Takashima et al., 0.76 V [62]. Table 1 highlights the performance of 16rGO-ZnO film compared with the standard IrO_2 and RuO_2 materials for oxygen evolution reaction.

The excellent electrocatalytic effect may be due to electrical contacts induced by good interaction of ZnO nanoparticles with the rGO functional groups. [30]. In the electrochemical process, the potential applied at the nanocomposite films interface promoted the formation of electron–hole pairs generated in the conduction and valence bands, respectively [69]. The presence of rGO in the nanocomposites increased charge separation of the electron-hole pairs [70], which allowed the higher electrocatalytic effect oxidation of water molecules by the holes to form O_2 when compared with pure ZnO film (Fig. 6(a)). Similarly, the improve of catalytic activity were reported by Suryanto, et al. [71], which related their results to catalytically active sites of Co_3O_4 and graphene, where the Co_3O_4 layer provided catalytically active sites for oxygen evolution and graphene promoted fast dissipation of the electrons generated during oxygen evolution.

The influence of pH on the electrochemical activity of films for water oxidation was also evaluated, as shown in Fig. 7(a–c). In the range of pH = 7.0 to 14.0, the anodic current was assignable to the O_2 evolution reaction, which the onset potential for water oxidation decreased for high pH values.

This pH dependence can suggest useful insight on the catalytic mechanism and intermediates of the reaction [72]. The assessed system, rGO-ZnO nanocomposites can act as an electrocatalyst for water oxidation process forming charged intermediates with low stability comparable to products [72]. In neutral pH the adsorption of H_2O molecules by rGO-ZnO surface (S) can occurs, forming an intermediate S-OH_2. Sequentially, the proton can thus to be transferred and the reaction proceeds through a charged interme-

Table 1
Comparative table on the OER performance of 16rGO-ZnO film compared with the standard IrO_2 and RuO_2 materials.

Catalyst	Synthesis method	Onset potential (V vs. Ag/AgCl) at neutral condition	Onset potential (V vs. Ag/AgCl) at alkaline condition	Ref.
IrO_2	commercial	–	0.61 V, (pH = 13.6)	[63]
IrO_2	commercial	–	0.57 V	[64]
IrOx	eletrodeposition	0.87 V, (pH = 7.0)	0.45, (pH = 13)	[65]
IrO_2	thermal oxidation	–	0.44 V, (pH = 13)	[66]
RuO_2	commercial	–	0.52 V, (pH = 13)	[67]
RuO_2	commercial	0.766 V, (pH = 7.4)	0.44, (pH = 14)	[68]
RuO_2	Commercial	–	0.56 V, (pH = 13.6)	[63]
RuO_2	commercial	–	0.51 V	[64]
RuO_2	thermal oxidation	–	0.44 V, (pH = 13)	[66]
16rGO-ZnO	microwave-hydrothermal	0.48 V, (pH = 7.0)	0.67 V, (pH = 13)	*this work*

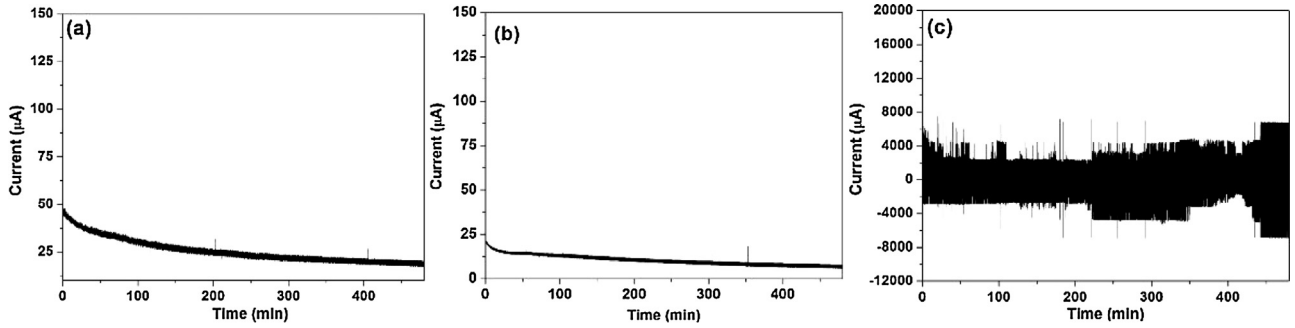

Fig. 8. Chronoamperometric tests for (a) ZnO pure (b) 8rGO-ZnO (c) 16rGO-ZnO nanocomposites films during 480 min of electrolysis at 1.40 V (vs. Ag/AgCl).

diate $[S—OH]^-$. One electron and one proton from $[S—OH]^-$ can be removed leading to the formation of an $[S—O]^-$ intermediate. This $[S\text{-}O]^-$ intermediate can interacts with other H_2O molecule followed by loss of one proton and one electron, generating $[S—OOH]^-$. This $[S—OOH]^-$ intermediate possibly deprotonates and another electron is transferred, which forms $[S\text{-}OO]^-$. The reaction proceeds and the O_2 molecules are obtained by loss of one electron with S-OO formation and posterior restoration of rGO-ZnO surface (S) (Fig. 6(b)) [72]. The addition of base was expected to promote an initial interaction of hydroxide ions with nanocomposite as the first step in the reaction, which lower energy cost required to form O_2 [73,74]. In this way, minimal potential can drive all of the PCET (proton-coupled electron-transfer) steps, avoiding thermodynamic barriers, where the overpotential is approximated by the free energy cost of the most demanding oxidation step by the formation of the first rGO-ZnO–oxo moiety [75]. The working potential range is often limited to the potential range in which water is stable, according to the Nernst equation, this range shifts by −59 mV for every increase of one pH unit [76].

To evaluate the stability of ZnO and rGO-ZnO nanocomposites films under catalytic turnover conditions, constant potential electrolysis experiments were applied at potential of 1.4 V in the presence of 0.1 mol L^{-1} phosphate buffer, pH = 7 (Fig. 8). The current density rapid decay at the early stages of the electrolysis, due rearrangement of surface active sites and instability of the catalyst particles [77]. The current then remained relatively constant for ZnO and 8rGO-ZnO electrodes (Fig. 8(a–b)), respectively. The 16rGO-ZnO nanocomposite electrode (Fig. 8(c)) presented a non-stationary behavior and highest current density during electrolysis, with accumulation of O_2 bubbles on its surface observed during the test (Fig. 7(d)). All catalyst electrodes show stable current density as function of time.

SEM images before and after the chronoamperometric tests are displayed in Fig. S2 (Supplementary Material). It is observed for pure ZnO and 8rGO-ZnO films that after the electrochemical process occurs a consuming of ZnO particles. It is important to note that despite 16rGO-ZnO present a slight decreasing of oxide amount on electrode surface after the application of potential application, there is no evidence of significant morphology change of the nanocomposite film. EDX analysis (Fig. S2; Supplementary Material) after the cronoamperometric measurements confirms the results obtained by SEM, showing the presence of intense peaks related to zinc, oxygen and carbon elements for 16rGO-ZnO film. These results evidence the importance of the amount of carbon material for the stability of the nanocomposite films.

4. Conclusions

In summary, rGO-ZnO nanocomposites were successful synthesized without any additional reducing reagents by microwave-hydrothermal method. According to the XRD analyses, Raman, XPS and infrared spectroscopy, GO were reduced under microwave-hydrothermal treatment, which is accompanied by formation of ZnO nanoparticles of about 110 nm distributed on rGO surface. The combination of ZnO nanoparticles and rGO enhanced electron transport, decreased the resistance of the films and facilitated the O_2 evolution reaction, with small overpotentials and higher catalytic current. The obtained results demonstrate that the rGO-ZnO nanocomposite films possess high electrical conductivity and electrocatalytic activity, promising characteristics in splitting of water for producing sustainable energy resources.

Acknowledgements

The authors are grateful to Coordenação de Aperfeiçoamento de Pessoal de Nível Superior (Capes), Financiadora de Estudos e Projetos (FINEP), Conselho Nacional de Desenvolvimento Científico e Tecnológico (CNPq), Fundação de Amparo à Pesquisa do Estado de Minas Gerais (FAPEMIG, under Grant no. APQ-00988-13), Rede Mineira de Química (RQ-MG) (FAPEMIG Project CEX-RED-00010-14) and Grupo de Materiais Inorgânicos do Triângulo – GMIT research group supported by FAPEMIG (APQ-00330-14) for the financial support. The authors would also like to thank Materials Chemistry Group at Federal University of Paraná for assistance in obtaining FEG-SEM images and Raman data, NUPE – Federal University of Uberlândia for EIS data, Multiuser Laboratory of

Chemistry Institute at the Universidade Federal de Uberlândia for providing the equipment and technical support for experiments involving scanning electron microscopy and EDX, to Prof. Valmor R. Mastelaro by the XPS measurements and Mr. Rorivaldo Camargo who operated TEM microscopy.

Appendix A. Supplementary data

Supplementary data associated with this article can be found, in the online version, at http://dx.doi.org/10.1016/j.apsusc.2017.06.221.

References

[1] S. Haussener, S. Hu, C. Xiang, A.Z. Weber, N.S. Lewis, Simulations of the irradiation and temperature dependence of the efficiency of tandem photoelectrochemical water-splitting systems, Energy Environ. Sci. 6 (2013) 3605–3618.
[2] J.L. Shi, J.M. Hu, Y.L. Luo, X.P. Sun, A.M. Asiri, Ni_3Se_2 film as a non-precious metal bifunctional electrocatalyst for efficient water splitting, Catal. Sci. Technol. 5 (2015) 4954–4958.
[3] H. Lei, A. Han, F. Li, M. Zhang, Y. Han, P. Du, W. Lai, R. Cao, Electrochemical, spectroscopic and theoretical studies of a simple bifunctional cobalt corrole catalyst for oxygen evolution and hydrogen production, Phys. Chem. Chem. Phys. 16 (2014) 1883–1893.
[4] A. Sartorel, M. Carraro, F.M. Toma, M. Prato, M. Bonchio, Shaping the beating heart of artificial photosynthesis: oxygenic metal oxide nano-clusters, Energy Environ. Sci. 5 (2012) 5592–5603.
[5] M.W. Kanan, D.G. Nocera, In situ formation of an oxygen-evolving catalyst in neutral water containing phosphate and Co^{2+}, Science 321 (2008) 1072–1075.
[6] Q. Yin, J.M. Tan, C. Besson, Y.V. Geletii, D.G. Musaev, A.E. Kuznetsov, Z. Luo, K.I. Hardcastle, C.L. Hill, A fast soluble carbon-free molecular water oxidation catalyst based on abundant metals, Science 328 (2010) 342–345.
[7] Y. Gao, H. Zhao, D. Chen, C. Chen, F. Ciucci, In situ synthesis of mesoporous manganese oxide/sulfur-doped graphitized carbon as a bifunctional catalyst for oxygen evolution/reduction reactions, Carbon 94 (2015) 1028–1036.
[8] F. Cheng, J. Chen, Metal-air batteries: from oxygen reduction electrochemistry to cathode catalysts, Chem. Soc. Rev. 41 (2012) 2172–2192.
[9] Y. Lee, J. Suntivich, K.J. May, E.E. Perry, Y. Shao-Horn, Synthesis and activities of rutile IrO_2 and RuO_2 nanoparticles for oxygen evolution in acid and alkaline solutions, J. Phys. Chem. Lett. 3 (2012) 399–404.
[10] J. Suntivich, K.J. May, H.A. Gasteiger, J.B. Goodenough, Y. Shao-Horn, A perovskite oxide optimized for oxygen evolution catalysis from molecular orbital principles, Science 334 (2011) 1383–1385.
[11] S. Stankovich, D.A. Dikin, G.H.B. Dommett, K.M. Kohlhaas, E.J. Zimney, E.A. Stach, R.D. Piner, S.T. Nguyen, R.S. Ruoff, Graphene-based composite materials, Nature 442 (2006) 282–286.
[12] Y. Zhu, S. Murali, W. Cai, X. Li, J.W. Suk, J.R. Potts, R.S. Ruoff, Graphene and graphene oxide: synthesis, properties, and applications, Adv. Mater. 22 (2010) 3906–3924.
[13] A.A. Balandin, S. Ghosh, W. Bao, I. Calizo, D. Teweldebrhan, F. Miao, C.N. Lau, Superior thermal conductivity of single-layer graphene, Nano Lett. 8 (2008) 902–907.
[14] A.K. Geim, K.S. Novoselov, The rise of graphene, Nat. Mater. 6 (2007) 183–191.
[15] S.-X. Guo, Y. Liu, A.M. Bond, J. Zhang, P.E. Karthik, I. Maheshwaran, S.S. Kumar, K.L.N. Phani, Facile electrochemical co-deposition of a graphene-cobalt nanocomposite for highly efficient water oxidation in alkaline media: direct detection of underlying electron transfer reactions under catalytic turnover conditions, Phys. Chem. Chem. Phys. 16 (2014) 19035–19045.
[16] S.-X. Guo, Y. Liu, C.-Y. Lee, A.M. Bond, J. Zhang, Y.V. Geletii, C.L. Hill, Graphene-supported [{$Ru_4O_4(OH)_{(2)}(H_2O)_{(4)}$}-(gamma-$SiW_{10}O_{36})_{(2)}$]10- for highly efficient electrocatalytic water oxidation, Energy Environ. Sci. 6 (2013) 2654–2663.
[17] J.M. Wang, W.R. Yang, J.Q. Liu, CoP_2 nanoparticles on reduced graphene oxide sheets as a super-efficient bifunctional electrocatalyst for full water splitting, J. Mater. Chem. A 4 (2016) 4686–4690.
[18] S. Chen, J.J. Duan, J.R. Ran, S.Z. Qiao, Paper-based N-doped carbon films for enhanced oxygen evolution electrocatalysis, Adv. Sci. 2 (2015) 1–5.
[19] T. Lv, L.K. Pan, X.J. Liu, Z. Sun, Enhanced photocatalytic degradation of methylene blue by ZnO-reduced graphene oxide-carbon nanotube composites synthesized via microwave-assisted reaction, Catal. Sci. Technol. 2 (2012) 2297–2301.
[20] F.C. Romeiro, J.Z. Marinho, S.C.S. Lemos, A.P. de Moura, P.G. Freire, L.E. da Silva, E. Longo, R.A.A. Munoz, R.C. Lima, Rapid synthesis of Co, Ni co-doped ZnO nanoparticles: optical and electrochemical properties, J. Solid State Chem. 230 (2015) 343–349.
[21] Y. Sun, Z.C. Shen, S.L. Xin, L. Ma, C.H. Xiao, S.J. Ding, F. Li, G.X. Gao, Ultrafine Co-doped ZnO nanoparticles on reduced graphene oxide as an efficient electrocatalyst for oxygen reduction reaction, Electrochim. Acta 224 (2017) 561–570.
[22] F.C. Romeiro, J.Z. Marinho, A.C.A. Silva, N.F. Cano, N.O. Dantas, R.C. Lima, Photoluminescence and magnetism in Mn^{2+}-doped ZnO nanostructures grown rapidly by the microwave hydrothermal method, J. Phys. Chem. C 117 (2013) 26222–26227.
[23] Q. Zhang, C.S. Dandeneau, X. Zhou, G. Cao, ZnO nanostructures for dye-sensitized solar cells, Adv. Mater. 21 (2009) 4087–4108.
[24] X. Dong, P. Yang, Y. Liu, C. Jia, D. Wang, J. Wang, L. Chen, Q. Che, Morphology evolution of one-dimensional ZnO nanostructures towards enhanced photocatalysis performance, Ceram. Int. 42 (2016) 518–526.
[25] C. Abed, C. Bouzidi, H. Elhouichet, B. Gelloz, M. Ferid, Mg doping induced high structural quality of sol-gel ZnO nanocrystals: application in photocatalysis, Appl. Surf. Sci. 349 (2015) 855–863.
[26] X.G. Chen, Y.Q. He, Q. Zhang, L.J. Li, D.H. Hu, Structure and photocatalytic properties of ZnO/RGO composite, Chin. J. Inorg. Chem. 25 (2009) 1953–1959.
[27] Y. Shen, S.C. Luo, Z.R. Wu, M. Cao, F. Gu, L.J. Wang, Preparation and sensing properties of mesoporous ZnO-rGO composites based on in situ hydrothermal synthesis, J. Mater. Sci. Mater. Electron. 27 (2016) 12660–12668.
[28] F.E. Osterloh, Inorganic materials as catalysts for photochemical splitting of water, Chem. Mater. 20 (2008) 35–54.
[29] T. Lu, Y.P. Zhang, H.B. Li, L.K. Pan, Y.L. Li, Z. Sun, Electrochemical behaviors of graphene-ZnO and graphene-SnO2 composite films for supercapacitors, Electrochim. Acta 55 (2010) 4170–4173.
[30] Y.-L. Chen, Z.-A. Hu, Y.-Q. Chang, H.-W. Wang, Z.-Y. Zhang, Y.-Y. Yang, H.-Y. Wu, Zinc oxide/reduced graphene oxide composites and electrochemical capacitance enhanced by homogeneous incorporation of reduced graphene oxide sheets in zinc oxide matrix, J. Phys. Chem. C 115 (2011) 2563–2571.
[31] M. Azarang, A. Shuhaimi, R. Yousefi, M. Sookhakian, Effects of graphene oxide concentration on optical properties of ZnO/RGO nanocomposites and their application to photocurrent generation, J. Appl. Phys. 116 (2014) 084306–084307.
[32] R.C. Lima, L.R. Macario, J.W.M. Espinosa, V.M. Longo, R. Erlo, N.L. Marana, J.R. Sambrano, M.L. dos Santos, A.P. Moura, P.S. Pizani, J. Andres, E. Longo, J.A. Varela, Toward an understanding of intermediate- and short-range defects in ZnO single crystals. A combined experimental and theoretical study, J. Phys. Chem. A 112 (2008) 8970–8978.
[33] J.Z. Marinho, L.M. Santos, L.R. Macario, E. Longo, A.E.H. Machado, A.O.T. Patrocinio, R.C. Lima, Rapid preparation of $(BiO)_{(2)}CO_3$ nanosheets by microwave-assisted hydrothermal method with promising photocatalytic activity under UV–vis light, J. Braz. Chem. Soc. 26 (2015) 498–505.
[34] N.P. Herring, S.H. Almahoudi, C.R. Olson, M.S. El-Shall, Enhanced photocatalytic activity of ZnO-graphene nanocomposites prepared by microwave synthesis, J. Nanopart. Res. 14 (2012) 1–13.
[35] W.S. Hummers, R.E. Offeman, Preparation of graphitic oxide, J. Am. Chem. Soc. 80 (1958) 1339.
[36] V.H.R. Souza, S. Husmann, E.G.C. Neiva, F.S. Lisboa, L.C. Lopes, R.V. Salvatierra, A.J.G. Zarbin, Flexible, transparent and thin films of carbon nanomaterials as electrodes for electrochemical applications, Electrochim. Acta 197 (2016) 200–209.
[37] E.G.C. Neiva, M.M. Oliveira, M.F. Bergamini, L.H. Marcolino, A.J.G. Zarbin, One material, multiple functions: graphene/$Ni(OH)_{(2)}$ thin films applied in batteries electrochromism and sensors, Sci. Rep. 6 (2016) 1–14.
[38] R.V. Salvatierra, M.M. Oliveira, A.J.G. Zarbin, One-pot synthesis and processing of transparent, conducting, and freestanding carbon nanotubes/polyaniline composite films, Chem. Mater. 22 (2010) 5222–5234.
[39] T. Huynh Ngoc, L. Van Hoang, H. Le Thuy, K. Nguyen Tri, S.H. Hahn, J.S. Chung, E.W. Shin, S.H. Hur, One-pot synthesis of a reduced graphene oxide-zinc oxide sphere composite and its use as a visible light photocatalyst, Chem. Eng. J. 229 (2013) 126–133.
[40] X. Chen, Y. He, Q. Zhang, L. Li, D. Hu, T. Yin, Fabrication of sandwich-structured ZnO/reduced graphite oxide composite and its photocatalytic properties, J. Mater. Sci. 45 (2010) 953–960.
[41] Q.-P. Luo, X.-Y. Yu, B.-X. Lei, H.-Y. Chen, D.-B. Kuang, C.-Y. Su, Reduced graphene oxide-hierarchical ZnO hollow sphere composites with enhanced photocurrent and photocatalytic activity, J. Phys. Chem. C 116 (2012) 8111–8117.
[42] M. Azarang, A. Shuhaimi, R. Yousefi, S.P. Jahromi, One-pot sol-gel synthesis of reduced graphene oxide uniformly decorated zinc oxide nanoparticles in starch environment for highly efficient photodegradation of methylene blue, RSC Adv. 5 (2015) 21888–21896.
[43] S.-S. Lo, D. Huang, C.-H. Tu, D.-J. Jan, Formation and Raman scattering of seed-like ZnO nanostructure, J. Raman Spectrosc. 40 (2009) 1694–1697.
[44] M. Scepanovic, M. Grujic-Brojcin, K. Vojisavljevic, S. Bernik, T. Sreckovic, Raman study of structural disorder in ZnO nanopowders, J. Raman Spectrosc. 41 (2010) 914–921.
[45] S. Ghosh, K. Ganesan, S.R. Polaki, T.R. Ravindran, N.G. Krishna, M. Kamruddin, A.K. Tyagi, Evolution and defect analysis of vertical graphene nanosheets, J. Raman Spectrosc. 45 (2014) 642–649.
[46] A.S.M.I. Uddin, G.-S. Chung, Synthesis of highly dispersed ZnO nanoparticles on graphene surface and their acetylene sensing properties, Sens. Actuators, B 205 (2014) 338–344.
[47] P. Jayabal, S. Gayathri, V. Sasirekha, J. Mayandi, V. Ramakrishnan, Preparation and characterization of ZnO/graphene nanocomposite for improved photovoltaic performance, J. Nanopart. Res. 16 (2014) 1–9.
[48] K. Huang, Y.H. Li, S. Lin, C. Liang, H. Wang, C.X. Ye, Y.J. Wang, R. Zhang, D.Y. Fan, H.J. Yang, Y.G. Wang, M. Lei, A facile route to reduced graphene oxide-zinc oxide nanorod composites with enhanced photocatalytic activity, Powder Technol. 257 (2014) 113–119.

[49] M.K. Han, X.W. Yin, L. Kong, M. Li, W.Y. Duan, L.T. Zhang, L.F. Cheng, Graphene-wrapped ZnO hollow spheres with enhanced electromagnetic wave absorption properties, J. Mater. Chem. A 2 (2014) 16403–16409.
[50] A. Esfandiar, S. Ghasemi, A. Irajizad, O. Akhavan, M.R. Gholami, The decoration of TiO2/reduced graphene oxide by Pd and Pt nanoparticles for hydrogen gas sensing, Int. J. Hydrogen Energy 37 (2012) 15423–15432.
[51] Y.C. Chen, K. Katsumata, Y.H. Chiu, K. Okada, N. Matsushita, Y.J. Hsu, ZnO-graphene composites as practical photocatalysts for gaseous acetaldehyde degradation and electrolytic water oxidation, Appl. Catal., A 490 (2015) 1–9.
[52] Q.W. Tang, L.H. Jiang, J. Liu, S.L. Wang, G.Q. Sun, Effect of surface manganese valence of manganese oxides on the activity of the oxygen reduction reaction in alkaline media, ACS Catal. 4 (2014) 457–463.
[53] J. Kim, C.L. Jung, M. Kim, S. Kim, Y. Kang, H.S. Lee, J. Park, Y. Jun, D. Kim, Electrocatalytic activity of NiO on silicon nanowires with a carbon shell and its application in dye-sensitized solar cell counter electrodes, Nanoscale 8 (2016) 7761–7767.
[54] T. Xu, L. Zhang, H. Cheng, Y. Zhu, Significantly enhanced photocatalytic performance of ZnO via graphene hybridization and the mechanism study, Appl. Catal., B 101 (2011) 382–387.
[55] A.P. de Moura, R.C. Lima, M.L. Moreira, D.P. Volanti, J.W.M. Espinosa, M.O. Orlandi, P.S. Pizani, J.A. Varela, E. Longo, ZnO architectures synthesized by a microwave-assisted hydrothermal method and their photoluminescence properties, Solid State Ionics 181 (2010) 775–780.
[56] N. Van Hoa, N. Thi Toan, J.-J. Shim, Rapid one-step synthesis and electrochemical properties of graphene/carbon nanotubes/MnO2 composites, Synth. Met. 199 (2015) 276–279.
[57] J. Ding, S. Zhu, T. Zhu, W. Sun, Q. Li, G. Wei, Z. Su, Hydrothermal synthesis of zinc oxide-reduced graphene oxide nanocomposites for an electrochemical hydrazine sensor, RSC Adv. 5 (2015) 22935–22942.
[58] L. Kashinath, K. Namratha, K. Byrappa, Microwave assisted facile hydrothermal synthesis and characterization of zinc oxide flower grown on graphene oxide sheets for enhanced photodegradation of dyes, Appl. Surf. Sci. 357 (2015) 1849–1856.
[59] D.K. Dogutan, R. McGuire Jr., D.G. Nocera, Electocatalytic water oxidation by cobalt(III) hangman beta-octafluoro corroles, J. Am. Chem. Soc. 133 (2011) 9178–9180.
[60] Y.F. Zhao, S.Q. Chen, B. Sun, D.W. Su, X.D. Huang, H. Liu, Y.M. Yan, K.N. Sun, G.X. Wang, Graphene-Co_3O_4 nanocomposite as electrocatalyst with high performance for oxygen evolution reaction, Sci. Rep. 5 (2015) 1–7.
[61] Y.Z. Han, Y.Z. Wu, W.Z. Lai, R. Cao, Electrocatalytic water oxidation by a water-soluble nickel porphyrin complex at neutral pH with low overpotential, Inorg. Chem. 54 (2015) 5604–5613.
[62] T. Takashima, K. Hashimoto, R. Nakamura, Inhibition of charge disproportionation of MnO2 electrocatalysts for efficient water oxidation under neutral conditions, J. Am. Chem. Soc. 134 (2012) 18153–18156.
[63] C.W. Tung, Y.Y. Hsu, Y.P. Shen, Y.X. Zheng, T.S. Chan, H.S. Sheu, Y.C. Cheng, H.M. Chen, Reversible adapting layer produces robust single-crystal electrocatalyst for oxygen evolution, Nat. Commun. 6 (2015) 1–9.
[64] Q. Wang, W.H. Hu, Y.M. Huang, Nitrogen doped graphene anchored cobalt oxides efficiently bi-functionally catalyze both oxygen reduction reaction and oxygen revolution reaction, Int. J. Hydrogen Energy 42 (2017) 5899–5907.
[65] T. Nakagawa, C.A. Beasley, R.W. Murray, Efficient electro-oxidation of water near its reversible potential by a mesoporous IrO_x nanoparticle film, J. Phys. Chem. C 113 (2009) 12958–12961.
[66] Y. Lee, J. Suntivich, K.J. May, E.E. Perry, Y. Shao-Horn, Synthesis and activities of rutile IrO_2 and RuO_2 nanoparticles for oxygen evolution in acid and alkaline solutions, J. Phys. Chem. Lett. 3 (2012) 399–404.
[67] M.R. Gao, X. Cao, Q. Gao, Y.F. Xu, Y.R. Zheng, J. Jiang, S.H. Yu, Nitrogen-doped graphene supported CoSe2 nanobelt composite catalyst for efficient water oxidation, Acs Nano 8 (2014) 3970–3978.
[68] T. Bhowmik, M.K. Kundu, S. Barman, Growth of one-dimensional RuO_2 nanowires on g-carbon nitride: an active and stable bifunctional electrocatalyst for hydrogen and oxygen evolution reactions at all pH values, ACS Appl. Mater. Interfaces 8 (2016) 28678–28688.
[69] A.J. Bard, M.A. Fox, Artificial photosynthesis – solar splitting of water to hydrogen and oxygen, Acc. Chem. Res. 28 (1995) 141–145.
[70] W.Q. Fan, X.Q. Yu, H.C. Lu, H.Y. Bai, C. Zhang, W.D. Shi, Fabrication of TiO_2/RGO/Cu_2O heterostructure for photoelectrochemical hydrogen production, Appl. Catal., B. 181 (2016) 7–15.
[71] B.H.R. Suryanto, X. Lu, C. Zhao, Layer-by-layer assembly of transparent amorphous Co_3O_4 nanoparticles/graphene composite electrodes for sustained oxygen evolution reaction, J. Mater. Chem. A 1 (2013) 12726–12731.
[72] L. Giordano, B. Han, M. Risch, W.T. Hong, R.R. Rao, K.A. Stoerzinger, Y. Shao-Horn, pH dependence of OER activity of oxides: current and future perspectives, Catal. Today 262 (2016) 2–10.
[73] H. Dau, C. Limberg, T. Reier, M. Risch, S. Roggan, P. Strasser, The mechanism of water oxidation: from electrolysis via homogeneous to biological catalysis, ChemCatChem 2 (2010) 724–761.
[74] Y. Meng, W. Song, H. Huang, Z. Ren, S.-Y. Chen, S.L. Suib, Structure-property relationship of bifunctional MnO_2 nanostructures: highly efficient, ultra-stable electrochemical water oxidation and oxygen reduction reaction catalysts identified in alkaline media, J. Am. Chem. Soc. 136 (2014) 11452–11464.
[75] S. Piccinin, A. Sartorel, G. Aquilanti, A. Goldoni, M. Bonchio, S. Fabris, Water oxidation surface mechanisms replicated by a totally inorganic tetraruthenium-oxo molecular complex, Proc. Natl. Acad. Sci. USA 110 (2013) 4917–4922.
[76] J.S. Spendelow, A. Wieckowski, Electrocatalysis of oxygen reduction and small alcohol oxidation in alkaline media, Phys. Chem. Chem. Phys. 9 (2007) 2654–2675.
[77] J. Tayal, B. Rawat, S. Basu, Bi-metallic and tri-metallic Pt-Sn/C, Pt-Ir/C, Pt-Ir-Sn/C catalysts for electro-oxidation of ethanol in direct ethanol fuel cell, Int. J. Hydrogen Energy 36 (2011) 14884–14897.